



# Highly Bi-doped Cu thin films with large spin-mixing conductance

Cite as: APL Mater. 6, 101107 (2018); <https://doi.org/10.1063/1.5049944>

Submitted: 26 July 2018 . Accepted: 03 October 2018 . Published Online: 22 October 2018

Sandra Ruiz-Gómez,  Aída Serrano, Rubén Guerrero, Manuel Muñoz, Irene Lucas, Michael Foerster, Lucía Aballe, José F. Marco, Mario Amado, Lauren McKenzie-Sell,  Angelo di Bernardo, Jason W. A. Robinson, Miguel Ángel González Barrio, Arantzazu Mascaraque, and Lucas Pérez



View Online



Export Citation



CrossMark

## ARTICLES YOU MAY BE INTERESTED IN

[Efficient spin current generation and suppression of magnetic damping due to fast spin ejection from nonmagnetic metal/indium-tin-oxide interfaces](#)


APL Materials **6**, 101105 (2018); <https://doi.org/10.1063/1.5050848>

[Recent advances in spin-orbit torques: Moving towards device applications](#)

Applied Physics Reviews **5**, 031107 (2018); <https://doi.org/10.1063/1.5041793>

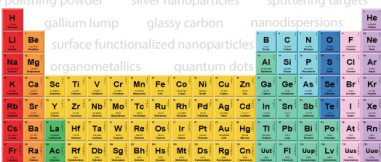
[Spin-orbit torque and spin pumping in YIG/Pt with interfacial insertion layers](#)

Applied Physics Letters **112**, 182406 (2018); <https://doi.org/10.1063/1.5025623>



**AMERICAN ELEMENTS**

THE ADVANCED MATERIALS MANUFACTURER®



additive manufacturing   epitaxial crystal growth   cerium oxide polishing powder   silver nanoparticles   sputtering targets   III-IV semiconductors   CVD precursors   europium phosphors

Li Be   gallium lump   glassy carbon   nanodispersions   He

Na Mg   surface functionalized nanoparticles   organometallics   quantum dot   Al Si P S Cl Ar

K Ca Sc Ti V Cr Mn Fe Co Ni Cu Zn Ga Ge As Se Br Kr

Rb Sr Y Zr Nb Mo Tc Ru Rh Pd Ag Cd In Sn Sb Te I Xe

Cs Ba La Hf Ta W Re Os Ir Pt Au Hg Tl Pb Bi Po At Rn

Fr Ra Ac Rf Db Sg Bh Hl Mt Ds Rg Cn Uut Fl Uuq Lv Uuq Uuq

deposition slugs   OLED Lighting   spintronics   solar energy

osmium   nanoribbons   thin films   chalcogenides   AuNPs

GDC   Li-ion battery electrolytes   99.999% ruthenium spheres

endohedral fullerenes   copper nanoparticles   diamond micropowder

CIGS   MBE grade materials   palladium catalysts   flexible electronics

beta-barium borate   borosilicate glass   dysprosium pellets   YBCO

pyrolytic graphite   3d graphene foam   indium tin oxide   mesoporous silica

raman substrates   sapphire windows   tungsten carbide   InGaAs

barium fluoride   carbon nanotubes   lithium niobate   scandium powder

perovskite crystals   yttrium iron garnet   alternative energy   h-BN

gold nanocubes   graphene oxide   macromolecules   photonics

rhodium sponge   fiber optics   beamsplitters   infrared dyes   zeolites

fused quartz   metallocenes   platinum ink   buckyballs   Ti-6Al-4V

**Now Invent.™**

The Next Generation of Material Science Catalogs

[www.americanelements.com](http://www.americanelements.com)

*American Elements opens up a world of possibilities so you can **Now Invent!***

Over 15,000 certified high purity laboratory chemicals, metals, & advanced materials and a state-of-the-art Research Center. Printable GHS-compliant Safety Data Sheets. Thousands of new products. And much more. All on a secure multi-language "Mobile Responsive" platform.



## Highly Bi-doped Cu thin films with large spin-mixing conductance

Sandra Ruiz-Gómez,<sup>1</sup> Aída Serrano,<sup>2</sup> Rubén Guerrero,<sup>3</sup> Manuel Muñoz,<sup>4</sup> Irene Lucas,<sup>5,6</sup> Michael Foerster,<sup>7</sup> Lucia Aballe,<sup>7</sup> José F. Marco,<sup>8,9</sup> Mario Amado,<sup>10</sup> Lauren McKenzie-Sell,<sup>10</sup> Angelo di Bernardo,<sup>10</sup> Jason W. A. Robinson,<sup>10</sup> Miguel Ángel González Barrio,<sup>1,9</sup> Arantazu Mascaraque,<sup>1,9</sup> and Lucas Pérez<sup>1,3,9</sup>

<sup>1</sup>*Departamento de Física de Materiales, Universidad Complutense de Madrid, 28040 Madrid, Spain*

<sup>2</sup>*SpLine, Spanish CRG BM25 Beamline, ESRF, 38000 Grenoble, France*

<sup>3</sup>*Instituto Madrileño de Estudios Avanzados, IMDEA Nanociencia, 28049 Madrid, Spain*

<sup>4</sup>*Instituto de Micro y Nanotecnología (CNM-CSIC), PTM, 28760 Tres Cantos, Madrid, Spain*

<sup>5</sup>*Departamento de Física de la Materia Condensada, Universidad de Zaragoza, Pedro Cerbuna, 12, 50009 Zaragoza, Spain*

<sup>6</sup>*Instituto de Nanociencia de Aragón (INA), Universidad de Zaragoza, Mariano Esquillor, Edificio I+D, 50018 Zaragoza, Spain*

<sup>7</sup>*Alba Synchrotron Light Facility, CELLS, Carrer de la Llum, 2-23, E-08290 Bellaterra, Spain*

<sup>8</sup>*Instituto de Química Física Rocasolano, CSIC, Calle de Serrano, 119, 28006 Madrid, Spain*

<sup>9</sup>*Unidad Asociada IQFR (CSIC)-UCM, 28040 Madrid, Spain*

<sup>10</sup>*Department of Materials Science and Metallurgy, University of Cambridge, 27 Charles Babbage Road, Cambridge CB3 0FS, United Kingdom*

(Received 26 July 2018; accepted 3 October 2018; published online 22 October 2018)

The spin Hall effect (SHE) provides an efficient tool for the production of pure spin currents, essentially for the next generation of spintronics devices. Giant SHE has been reported in Cu doped with 0.5% Bi grown by sputtering, and larger values are predicted for larger Bi doping. In this work, we demonstrate the possibility of doping Cu with up to 10% of Bi atoms without evidence of Bi surface segregation or cluster formation. In addition, YIG/BiCu structures have been grown, showing a spin mixing conductance larger than the one shown by similar Pt/YIG structures, reflecting the potentiality of these new materials. © 2018 Author(s). All article content, except where otherwise noted, is licensed under a Creative Commons Attribution (CC BY) license (<http://creativecommons.org/licenses/by/4.0/>). <https://doi.org/10.1063/1.5049944>

Spintronics studies and exploits the intrinsic spin of the electron and its associated magnetic moment jointly with its fundamental charge for the generation, manipulation, and detection of spin currents that can be implemented in solid state devices.<sup>1</sup> In particular, the possibility of harvesting pure spin currents, i.e., without charge current, and using them in memory-logic devices plays a key role in the next generation of electronics due to the expected low power consumption.<sup>2,3</sup> In this regard, the spin Hall effect (SHE) provides an efficient tool for the conversion of a charge current into a spin current in nonmagnetic materials without any associated current injection from the ferromagnets.<sup>4,5</sup> To exploit this effect, identifying novel materials with a large charge-to-spin conversion, i.e., materials with large spin Hall angles (SHAs) turn out to be essential.<sup>6-8</sup>

In addition to metals showing intrinsic SHE, giant SHE has been predicted when they are conveniently doped with impurities showing strong spin-orbit interactions.<sup>9,10</sup> In these materials, extrinsic scattering mechanisms such as skew scattering<sup>11</sup> and side jump effect<sup>12</sup> might also give rise to SHE. In fact, a SHA of  $\sim -0.24$  has been measured by Niimi and co-workers in CuBi alloys with  $\sim 0.5\%$  of Bi grown by sputtering.<sup>13</sup> The authors mentioned in the supplementary material of Ref. 13 that a larger Bi content leads to surface segregation. However, larger values of SHA are expected theoretically for higher doping of Bi in Cu.<sup>14</sup>

In this work, we demonstrate Bi doping of Cu films with up to 10% without surface segregation or cluster formation. When grown on yttrium iron garnet (YIG) substrates, the interfaces show a large

spin mixing conductance. These new materials open the possibility of studying the giant SHE and using it in future spintronics devices.

The first growth stages were studied at the CIRCE beamline<sup>15</sup> of the Alba synchrotron in Spain. The beamline experimental station chamber houses an Elmitec III Low-Energy Electron Microscope (LEEM) that allows for fast real-space imaging of the surface of the CuBi films during growth, as well as selected-area low energy electron diffraction (LEED) measurements. Samples for the LEEM experiments were grown *in situ* onto Ru(0001) single-crystal substrates that were cleaned by exposure to  $10^{-8}$  mbar of oxygen at 1000 K followed by flashing at 1500 K in vacuum. Afterwards, Bi and Cu were co-evaporated from electron-beam heated dosers, at a base pressure of  $1 \times 10^{-10}$  mbar. The Bi and Cu evaporation rates were adjusted to ensure that the Bi content in the film was below 10% in all experiments.

Thin films (25 nm) were grown by thermal evaporation in a High-Vacuum (HV) chamber with individual Joule dosers for Bi and Cu. The base pressure of the chamber was  $10^{-7}$  mbar. Previous to the film growth, the dosers were calibrated using a quartz crystal microbalance. The substrates were Si(100) wafers with native  $\text{SiO}_2$  and were kept at room temperature during growth.

A scanning electron microscope (SEM) JEOL JEM 6335 equipped with an energy dispersive X-ray (EDX) system was used to study the composition of the samples. The crystalline structure was studied by X-ray diffraction (XRD) with a grazing incidence angle of  $0.5^\circ$ , with a PANalytical X-ray diffractometer using  $\text{CuK}\alpha$  radiation. Scanning transmission electron microscopy (STEM) was performed in an FEI Titan 60 operated at 300 kV and equipped with a high brightness Schottky field emission gun. Z contrast imaging has been carried out in high angle annular dark field (HAADF) with a probe convergence angle of 25 mrad and an inner collection angle of 58 mrad. The specimens analyzed are lamellas extracted from the samples by focused ion beam (FIB) milling in a FEI Helios Nanolab 600.

X-ray Photoelectron Spectroscopy (XPS) data were recorded with a CLAM2 analyser under a base pressure of  $5 \times 10^{-9}$  mbar using Mg  $\text{K}\alpha$  radiation and a constant pass energy of 200 eV and 20 eV for the wide and narrow scan spectra, respectively. The binding energy scale was referenced to that of the C 1s signal of the adventitious contamination layer which was set at 284.6 eV. The samples were subjected to  $\text{Ar}^+$  sputtering to investigate the in-depth distribution of the different chemical elements. An integral  $\text{Ar}^+$  ion gun was used at 20 keV and 20 mA and an Ar pressure within the analysis chamber of  $5 \times 10^{-5}$  mbar.

X-ray absorption spectroscopy (XAS) measurements are carried out at the Cu K-edge (8.98 keV) and Bi  $\text{L}_3$ -edge (13.42 keV) at the beamline BM25A of the European Synchrotron (ESRF) in Grenoble (France). Bi and Cu foils were measured in transmission mode at the beginning of the experiment for energy calibration.  $\text{Cu}_2\text{O}$ ,  $\text{CuO}$ , and  $\text{Bi}_2\text{O}_3$  reference samples were also measured in transmission mode. Sample spectra were collected in fluorescence yield mode placing samples at  $45^\circ$  from the incoming X-ray beam and forming  $45^\circ$  with the dispersive X-ray fluorescence detector. From three to five spectra were acquired from each sample and merged in order to improve the signal-to-noise ratio. The acquisition time for each energy scan was about 40 min. XAS data were processed using the Demeter package and applying standard methods.<sup>16</sup>

Ferromagnetic resonance spectroscopy (FMR) was carried out at room temperature (RT) on BiCu (25 nm)/YIG(110) (43 nm) structures prepared as described in the [supplementary material](#). The samples were placed face down in a grounded coplanar waveguide in a wide band set up in order to excite the sample with the RF field. The DC external magnetic field was generated by an electromagnet and aligned perpendicular to the RF field and parallel to the sample (in-plane geometry). A microwave signal (constant power of  $-5$  dBm) was applied to the waveguide using a KEYSIGHT N9918A generator, and a diode KEYSIGHT 8473B was used for detection. Field modulation (0.6 Oe) and a lock-in amplifier were used to extract the derivative of the absorbed power versus DC field.

Bi has been widely used as a surfactant in the growth of metals in UHV vacuum conditions.<sup>17</sup> Therefore, as a first step, it is important to establish the growth conditions to avoid Bi migration to the film surface. We have therefore studied the first stages of growth of the model system Cu/Ru(0001) at different temperatures, incorporating Bi in Cu during growth while monitoring the process using the LEED pattern. Figure 1(a) shows the LEED pattern obtained during the growth at room-temperature. The spots observed in the LEED pattern correspond to the hexagonal ones of the Cu(111) on Ru

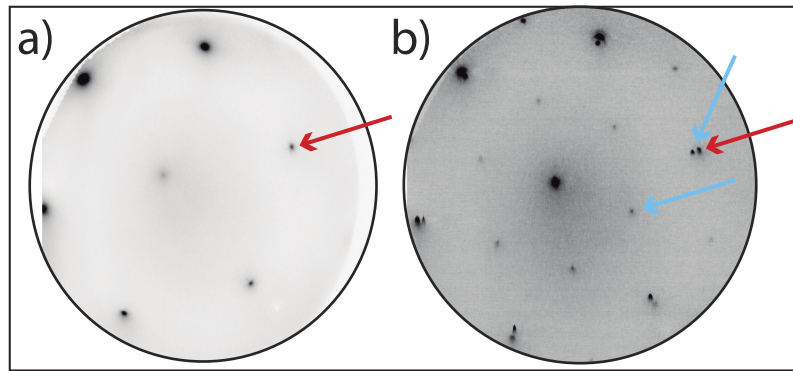


FIG. 1. (a) LEED pattern of a Cu(Bi) thin film grown on Ru(0001) at RT. (b) LEED pattern of a Cu(Bi) thin film grown on Ru(0001) at 100 °C. The red arrows mark the characteristic spots of Cu(111) on Ru(0001), and the blue arrows mark the spots of the  $(\sqrt{3} \times \sqrt{3})$  R30 reconstruction of Bi on Cu(111).

(marked with a red arrow). There are no extra-spots corresponding to Bi on a Cu surface, i.e., the Bi atoms are either not on the Cu surface or do not form an ordered structure. However, when Cu and Bi are co-evaporated at a higher temperature (100 °C) [Fig. 1(b)], additional LEED spots appear that can be related to a  $(\sqrt{3} \times \sqrt{3})$  R30° reconstruction, which is a characteristic of a Bi monolayer on the surface of a Cu(111).<sup>18</sup> From the LEED pattern, it is clear that, when growing at a high temperature, Bi segregates to the surface, whereas no segregation is observed at RT.

If these Bi-doped Cu films are intended to be used in spintronics, it is mandatory to grow them on substrates that allow for the realization of magnetotransport measurements. Taking this into account, samples were grown on SiO<sub>2</sub>/Si at RT. The Cu evaporation rate is kept constant at 0.4 Å/s, while the Bi evaporation rate was varied to obtain a Bi content in Cu from 1 wt. % to 40 wt. %—as measured by EDX. Pure Cu and Bi films were also grown as reference samples. EDX measurements reveal a homogeneous composition in all samples.

A first approach of the Bi distribution along the cross section of the BiCu films can be obtained from the XPS technique. Figure S1 collects the wide scan spectra recorded at different sputtering times from a Bi<sub>85</sub>Cu<sub>15</sub> sample. The spectra show only Cu, Bi, O, and C signals. As the sputtering time increases, the intensity of the C and O signals decreases strongly, while the Cu 2p peaks increase due to the removal of the contamination layer from the uppermost surface being really small after long sputtering times. The spectra also show a clear increase in the intensity of the Cu 2p peaks with increasing sputtering time. However, more than due to an increase in Cu concentration, this must be related to a much smaller, almost insignificant, attenuation of the Cu 2p electrons once the contamination layer has been removed from the uppermost surface (see below).

Cu/Bi and O/Cu atomic ratios were calculated from the integration of the Cu 2p, O 1s, and Bi 4f spectral areas after background subtraction (Shirley method) using the MultiQuant XPS software. This package allows taking into account the attenuation brought about by the adventitious carbon layer.<sup>19</sup> This is important in the present case, particularly for the Cu/Bi atomic ratio, since the Cu 2p and Bi 4f spectral regions are separated by approximately 800 eV and therefore the signal corresponding to the Cu 2p electrons, which have a much smaller kinetic energy than the Bi 4f ones, is significantly more attenuated by the contamination layer than that of the Bi 4f electrons. Figure 2(a) shows the Cu/Bi and O/Cu atomic ratios obtained from the XPS data. It is clear from Fig. 2 that the O/Cu ratio decreases rapidly with sputtering time, indicating that the surface oxidic layer is effectively removed by Ar<sup>+</sup> bombardment (XPS data, not shown, reveal that the most external part of the sample contains both Cu<sup>+</sup> and Bi<sup>3+</sup>). Contrarily, the Cu/Bi ratio remains fairly constant with sputtering time both within the oxidic surface layer and in the sample itself. Given the composition of the sample, the expected Cu/Bi atomic ratio should be 5.7 which is close, within the error of the experimental determination, to the value found in the current experiments. Therefore, in view of the present data, we can conclude that there is no enrichment either in Cu or Bi within the depth explored in this work.

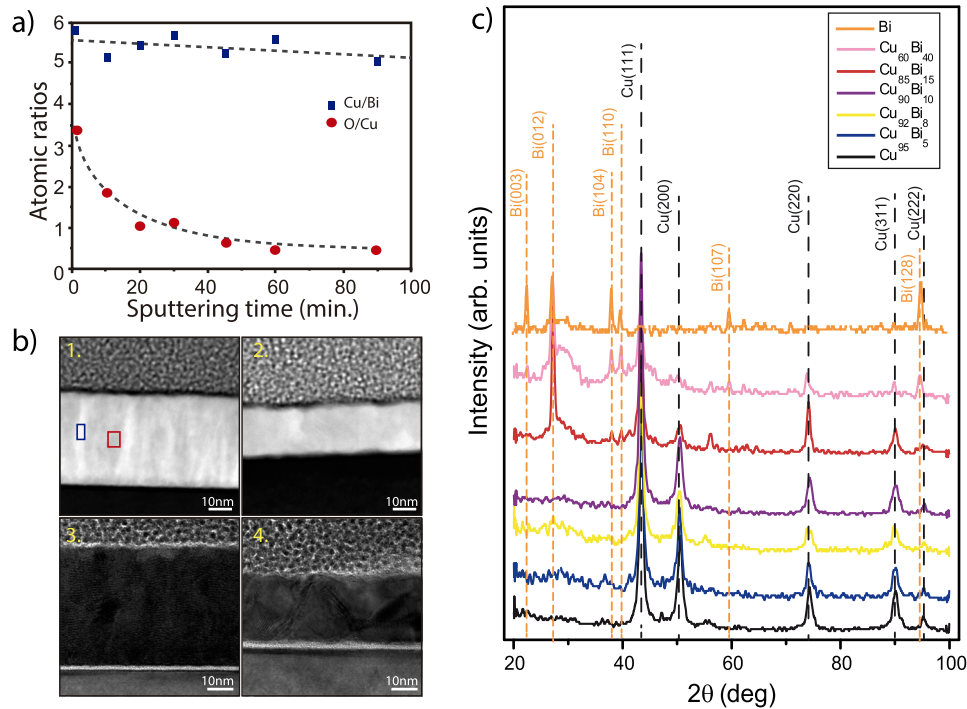


FIG. 2. (a) Atomic ratios obtained from the evaluation of the XPS data for a Cu<sub>85</sub>Bi<sub>15</sub> film. (b) (1) Z-contrast and (3) HR-TEM image of Cu<sub>75</sub>Bi<sub>25</sub>, (2) Z-contrast, and (4) HR-TEM image of Cu<sub>96</sub>Bi<sub>4</sub>. (c) XRD patterns for the Bi-doped samples under study. Reflections corresponding to the Cu-fcc spectrum are marked with gray dashed lines and the ones corresponding to the orthorhombic Bi structure with orange dashed lines.

Additional information on the distribution of Bi in the alloys can be extracted from cross-sectional high resolution TEM images. Panel 1 of Fig. 2(b) shows a TEM image with Z-contrast measured in the sample Cu<sub>75</sub>Bi<sub>25</sub>. Dark and light areas can be clearly distinguished, corresponding to zones with different composition. In particular, the blue square corresponds to a Bi-poor region (light area), whereas the red square to a Bi-rich region (dark area). From this image, a clear segregation of Bi in the sample is noted. However, the Z-contrast image measured in the sample Cu<sub>96</sub>Bi<sub>4</sub> [panel 2 of Fig. 2(b)] is much more homogeneous, without a clear contrast. In this case, Bi is distributed homogeneously across the entire sample. No Bi accumulation has been observed in either the top or bottom surfaces of the thin films. The high-resolution images [panels 3 and 4 in Fig. 2(b)] evidence the polycrystalline nature of the samples where the disorder increased with the Bi content.

The presence of large clusters can be explored by XRD. Considering the thickness of the films (below 50 nm in all cases), we have measured in grazing incidence configuration to reduce the signal from the substrate and get a better signal-to-noise ratio. Figure 2(c) collects the XRD patterns for the thin films under study, together with a Cu and Bi reference thin film. Reflections corresponding to the Cu-fcc structure are marked with black lines, the ones corresponding to the orthorhombic Bi structure with orange lines and the one marked with an asterisk corresponding to the Si substrate. As expected, Cu and Bi reference samples only show reflections that can be indexed as pure Cu or Bi, respectively. For low doped samples (Cu<sub>95</sub>Bi<sub>5</sub>, Cu<sub>92</sub>Bi<sub>8</sub>, and Cu<sub>90</sub>Bi<sub>10</sub>), we observe Cu(111), Cu(200), and Cu(220) reflections, the same as in the Cu reference. There is only a slight increase in the width of the peaks, probably due to the disorder induced in the Cu lattice by the incorporation of Bi atoms. No Bi reflections are detected. The Bi atoms seem incorporated into the fcc-Cu lattice. When increasing the doping level above 10%, see samples Cu<sub>85</sub>Bi<sub>15</sub> and Cu<sub>60</sub>Bi<sub>40</sub>, new reflections appear that can be indexed as Bi(012) and Bi(311). Thus, as expected, for high Bi doping, Bi agglomerates and clusters are detected by XRD.

To further investigate the structure of the films and to elucidate whether Bi clusters are formed into the Cu matrix, we employed X-ray absorption fine structure techniques, which are sensitive to the local atomic environment of X-ray absorbing atoms. Figure 3(a) displays the normalized X-ray

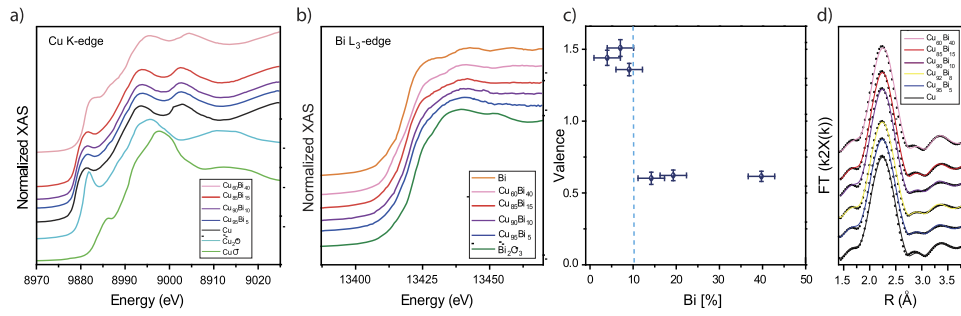


FIG. 3. (a) Normalized XANES spectra at the Cu K-edge of the different  $\text{Cu}_{1-x}\text{Bi}_x$  thin films together with the Cu,  $\text{Cu}_2\text{O}$ , and CuO reference samples. (b) Normalized XANES spectra at the Bi L<sub>3</sub>-edge of  $\text{Cu}_{1-x}\text{Bi}_x$  thin films and Bi and  $\text{Bi}_2\text{O}_3$  references. (c) Valence of the Bi atoms as a function of the Bi content of the alloys, calculated as described in the text. (d) Fourier transform function of the EXAFS signal (experimental and fitting) of films from the signal collected at the Cu K-edge.

absorption near edge structure (XANES) spectra at the Cu K-edge for the different  $\text{Cu}_x\text{Bi}_y$  thin films together with the Cu foil,  $\text{Cu}_2\text{O}$ , and CuO references. A close inspection of the different curves reveals that the incorporation of Bi does not change the shape of the spectra or the position of the energy edge unless the Bi content exceeds 15%. In the  $\text{Cu}_{60}\text{Bi}_{40}$  sample, a shift in the absorption edge and the resonances after the edge toward higher energies, as well as dissimilarities in the line shape, are observed. This might be a clear indication of the introduction of a large disorder in the Cu structure. To quantify the possible oxidation of the layers, the XANES spectra of the samples were fitted to a linear combination of the spectra of different reference samples. All samples show an oxide content around 8%, independent of the Bi doping. This oxide could be ascribed to a surface oxidation layer, as supported by the XPS data shown before. Visual examination of the XANES spectra measured at the Bi L<sub>3</sub>-edge [Fig. 3(b)] reinforces the idea of Bi diluted in the Cu matrix. Spectra corresponding to the samples with the Bi content below 15% are very different from the Bi reference sample as well as from the  $\text{Bi}_2\text{O}_3$  reference sample, which reflects a different local environment of the doping Bi atoms.

The mean valence of the Bi doping atoms in the structure can be calculated using Kunzl's law,<sup>20</sup> by linear interpolation of the shift of the edge position with respect to the absorption edge of Bi metallic and oxide references. The output of this interpolation as a function of the Bi content in the thin films is shown in Fig. 3(c). It is possible to see that, within the noise, there are only two sets of values for the valence related to Bi in the Cu matrix and Bi in the cluster form, with a limiting value around 10%. It is particularly noticeable that the value of the valence obtained for samples with a content of bismuth below 10%, a value close to 1.5, is in good agreement with the reported values obtained from *ab initio* calculations in homogeneously Bi-doped Cu films.<sup>21</sup>

Analysis of the Fourier transform (FT) of the extended X-ray absorption fine structure (EXAFS) spectra was performed for several Bi-doped Cu films as well as the Cu foil reference. A  $k^2$  weighting was used in the  $k$  range 2.7-13.0  $\text{\AA}^{-1}$  for fitting of FT signals in R space using theoretical functions from the FEFF code.<sup>22</sup> The experimental FT module and the fitting are shown in Fig. 3(d). Table I

TABLE I. Nearest neighbour structural parameters obtained by the FT  $k^2\chi(k)$  curve fitting for Cu foil reference and Cu(Bi) films. N is the coordination number that is fixed for the Cu foil reference,  $R_{\text{Cu-Cu}}$  is the average interatomic distance, and  $\sigma^2$  are the Debye-Waller factors.

| %Bi  | N        | $R_{\text{Cu-Cu}}$ ( $\text{\AA}$ ) | $\sigma^2$ ( $\times 10^{-3} \text{\AA}^2$ ) |
|------|----------|-------------------------------------|--|
| Foil | 12       | 2.544 (2)                           | 8.76 (9)                                     |
| 0    | 11.1 (2) | 2.543 (2)                           | 8.6 (1)                                      |
| 5    | 10.6 (1) | 2.542 (7)                           | 8.7 (1)                                      |
| 8    | 10.1 (1) | 2.542 (1)                           | 8.40 (9)                                     |
| 10   | 10.8 (1) | 2.543 (9)                           | 8.7 (1)                                      |
| 15   | 10.8 (1) | 2.544 (3)                           | 8.6 (1)                                      |
| 40   | 9.9 (2)  | 2.548 (5)                           | 9.0 (2)                                      |

displays the fitting structural parameters. FT  $k^2\chi(k)$  fitting of the first interatomic distance is very similar for all samples under study and to that of the Cu foil. Structural parameters obtained at the first Cu-Cu shell do not alter at local order the Cu structure except for the sample with a 40% Bi in which the incorporation of Bi atoms into the Cu lattice induces a slight decrease in the coordination number, an elongation of the Cu-Cu distance, and an increase in the Debye-Waller factor. Fitting of the second shell in each FT  $k^2\chi(k)$  spectrum was also performed. However these do not show a clear tendency with the Bi content. It seems that for a low Bi content, Bi atoms are incorporated in the Cu lattice, producing a distortion of it at larger local orders, which makes it difficult to analyze the second shell considering slight distortions of the Cu structure.

Finally, we performed FMR measurements on two YIG/BiCu heterostructures. The FMR was measured as described in the [supplementary material](#). In order to calculate the damping constant, the measurements were performed at different values of the excitation frequency.

Using Kittel's equation for in-plane measurements,<sup>23,24</sup> it is possible to obtain the values of effective saturation magnetization and the Landé gyromagnetic factor ( $g$ ). The continuous line in Fig. S3 corresponds to the fitting of experimental data using the equation

$$f = |\gamma| \sqrt{H_{\text{FMR}}(H_{\text{FMR}} + 4\pi M_s - H_{\text{ani}})}. \quad (1)$$

Regarding the YIG substrates whose measurements are shown in Fig. S2, we have found a  $4\pi M_s$  of 1730 G in the first case and of 1493 G in the second case. The value of the gyromagnetic ratio is 2.8 MHz/Oe in both cases, which is in good agreement with the reported values.<sup>24–27</sup> Plotting now the dependence of the linewidth with frequency, the damping can be calculated from the following equation:

$$\Delta H_{\text{FMR}} = \Delta H_0 + \frac{2\alpha f}{\sqrt{3}\gamma}. \quad (2)$$

Before studying the CuBi/YIG samples, we have measured FMR in Bi/YIG and Cu/YIG control samples following the same procedure used for CuBi/YIG. As shown in Fig. S3 ([supplementary material](#)), there is no increase in the damping of YIG when capped with Cu or Bi, and thus the spin-mixing conductance is negligible for these materials.

After capping YIG with a CuBi layer, a significant increase in the slope of the frequency-dependent linewidth and hence an increased Gilbert damping constant are observed (see Fig. 4). When a ferromagnetic layer as YIG is capped with a metallic layer as CuBi, the precession of the magnetization in the magnetic layer causes a flow of spins to the metallic layer because CuBi acts as a spin sink. Therefore, the damping constant for YIG/CuBi is the damping constant for uncapped YIG plus a contribution due to spin pumping  $\alpha_0 = \alpha + \alpha_{\text{sp}}$ . The damping obtained for both samples is summarized in Table II. Due to the conservation of angular momentum, this additional damping can be used to evaluate the CuBi/YIG interface spin-mixing conductance. The additional Gilbert damping

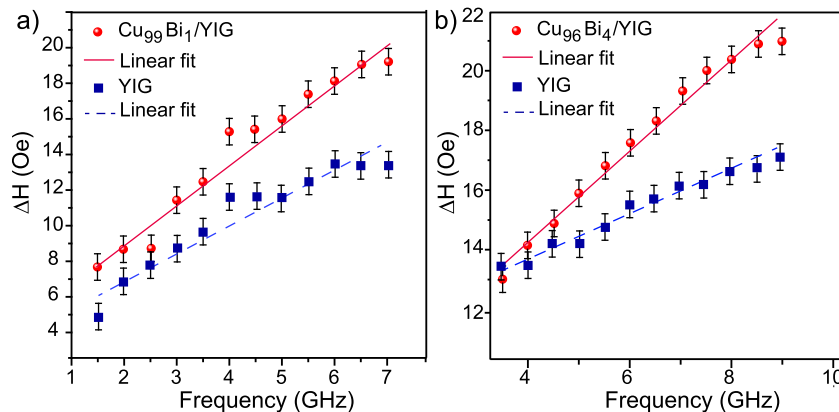


FIG. 4. (a) Frequency dependence of the FMR linewidth for sample  $\text{Cu}_{99}\text{Bi}_1$  after and before CuBi deposition and (b) sample  $\text{Cu}_{96}\text{Bi}_4$  after and before CuBi deposition.

TABLE II. Damping constants and spin mixing conductance for bare YIG substrates as well as for YIG/CuBi interfaces.

| Sample                           | $\alpha_{\text{YIG}} (\times 10^{-3})$ | $\alpha_{\text{YIG/CuBi}} (\times 10^{-3})$ | $\alpha_{\text{sp}} (\times 10^{-3})$ | $G_{\text{eff}} (\times 10^{18} \text{ m}^{-2})$ |
|----------------------------------|--|---|---------------------------------------|--|
| Cu <sub>99</sub> Bi <sub>1</sub> | 3.7 ± 0.2                              | 5.4 ± 0.2                                   | 1.7 ± 0.4                             | 7.1 ± 0.7  |
| Cu <sub>96</sub> Bi <sub>4</sub> | 1.7 ± 0.1                              | 3.7 ± 0.1                                   | 2.0 ± 0.2                             | 7.3 ± 0.5  |

is related to the effective interface spin-mixing conductance  $G_{\text{eff}}$  by the following relationship:<sup>25</sup>

$$\alpha_{\text{sp}} = \frac{g\mu_B 4\pi M_S G_{\text{eff}}}{t_{\text{YIG}}}, \quad (3)$$

where  $M_S$  is the saturation magnetization,  $t_{\text{YIG}}$  is the thickness of the magnetic material,  $g$  is the  $g$  factor, and  $\mu_B$  is the Bohr magneton. The spin mixing conductance obtained for both samples is summarized in Table II. These values are in the same range than the values measured in optimized Pt/YIG interfaces.<sup>28</sup>

To sum up, we have demonstrated that it is possible to incorporate up to 10% of Bi atoms into the Cu structure by co-evaporation of Bi and Cu atoms in a molecular beam epitaxy system at room temperature. Bi is incorporated in the Cu lattice, without any trace of segregation or cluster formation below 10% of Bi. There is also no presence of Cu or Bi oxides apart from the surface oxidation layer formed when the sample is exposed to air. Structural properties of Bi-doped Cu with up to 10% Bi are similar to the one of Cu, reflecting the incorporation of Bi in the Cu structure, forming an alloy. CuBi/YIG interfaces have also been studied by FMR. These interfaces show a large spin-mixing conductance, which opens the possibility of exploring the spin Hall effect of these alloys beyond the region explored up to date, expanding their possible use in spintronics.

See [supplementary material](#) for a description of the growth of the YIG substrates, the wide scan spectra for a Bi<sub>85</sub>Cu<sub>15</sub> sample, and additional FMR characterization of BiCu/YIG samples as well as Bi/YIG and Cu/YIG control samples.

This work has been partially funded by MAT2014-52477-C5, MAT2017-87072-C4, and MAT2015-64110-C2-2-P from the Ministerio de Ciencia e Innovación and Nanofrontmag from Comunidad de Madrid. IMDEA Nanociencia acknowledges support from the Severo Ochoa Programme for Centres of Excellence in R&D (MINECO, Grant No. SEV-2016-0686). We acknowledge the European Synchrotron Radiation Facility (ESRF), MINECO, and CSIC for provision of synchrotron radiation facilities, the BM25-SpLine staff for the technical support beyond their duties, and the financial support for the beamline (No. PIE-2010-OE-013-200014). We thank the Spanish National Center of Electron Microscopy for SEM measurements and the CAI de Difracción de Rayos X, Universidad Complutense de Madrid, for XRD measurements. The TEM work has been conducted in the Laboratorio de Microscopías Avanzadas (LMA) at the Instituto de Nanociencia de Aragón (INA)-Universidad de Zaragoza. The authors acknowledge the LMA-INA for offering access to their instruments and expertise. M.A. acknowledges MSCA-IFEF-ST No. 656485-Spin3. J.W.A.R. acknowledges Royal Society (Superconducting Spintronics), Leverhulme Trust (No. IN-2013-033).

<sup>1</sup> I. Zutic, J. Fabian, and S. Das Sarma, *Rev. Mod. Phys.* **76**, 323 (2004).

<sup>2</sup> F. Pullizi, *Nat. Mater.* **11**, 367 (2012).

<sup>3</sup> A. V. Chumak, V. I. Vasyuchka, A. A. Serga, and B. Hillebrands, *Nat. Phys.* **11**, 453 (2015).

<sup>4</sup> T. Jungwirth, J. Wunderlich, and K. Olejník, *Nat. Mater.* **11**, 382 (2012).

<sup>5</sup> J. Sinova, S. O. Valenzuela, J. Wunderlich, C. H. Back, and T. Jungwirth, *Rev. Mod. Phys.* **87**, 1213 (2015).

<sup>6</sup> T. Wang, W. Wang, Y. Xie, M. A. Warsi, J. Wu, Y. Chen, V. O. Lorenz, X. Fan, and J. Q. Xiao, *Sci. Rep.* **7**, 1036 (2017).

<sup>7</sup> J. Balakrishnan, G. K. W. Koon, A. Avsar, Y. Ho, J. H. Lee, M. Jaiswal, S. Baek, J. Ahn, A. Ferreira, M. A. Cazalilla, A. H. C. Neto, and B. Ozyilmaz, *Nat. Commun.* **5**, 4748 (2014).

<sup>8</sup> M. J. Jin, S. Y. Moon, J. Park, V. Modepalli, J. Jo, S.-I. Kim, H. C. Koo, B. Min, H. Lee, S. H. Baek, and J. W. Yoo, *Nano Lett.* **17**, 36 (2017).

<sup>9</sup> M. Gradhand, D. V. Fedorov, P. Zahn, and I. Mertig, *Phys. Rev. B* **81**, 245109 (2010).

<sup>10</sup> Y. Niimi and Y. Otani, *Rep. Prog. Phys.* **78**, 124501 (2015).

<sup>11</sup> C. Herschbach, D. V. Fedorov, I. Mertig, M. Gradhand, K. Chadova, H. Ebert, and D. Ködderitzsch, *Phys. Rev. B* **88**, 205102 (2013).

<sup>12</sup> A. Fert and P. M. Levy, *Phys. Rev. Lett.* **106**, 157208 (2011).



- <sup>13</sup> Y. Niimi, Y. Kawanishi, D. H. Wei, C. Deranlot, H. X. Yang, M. Chshiev, T. Valet, A. Fert, and Y. Otani, *Phys. Rev. Lett.* **109**, 156602 (2012).
- <sup>14</sup> D. V. Fedorov, C. Herschbach, A. Johansson, S. Ostanin, I. Mertig, M. Granhand, K. Chadova, D. Ködderitzsch, and H. Ebert, *Phys. Rev. B* **88**, 085116 (2013).
- <sup>15</sup> L. Aballe, M. Foerster, E. Pellegrin, J. Nicolas, and S. Ferrer, *J. Synchrotron Radiat.* **22**, 745 (2015).
- <sup>16</sup> B. Ravel and M. Newville, *J. Synchrotron Radiat.* **12**, 537 (2005).
- <sup>17</sup> E. C. Young, S. Tixier, and T. Tiedje, *J. Cryst. Growth* **279**, 316 (2005).
- <sup>18</sup> R. van Gastel, D. Kaminski, E. Vlieg, and B. Poelsema, *Phys. Rev. B* **89**, 075431 (2014).
- <sup>19</sup> M. Mohai, *Surf. Interface Anal.* **36**, 828 (2004).
- <sup>20</sup> C. Kittel, *Collection des Travaux Chimiques de Tchécoslovaquie* (Tiskárna "Politika," 1932), Vol. 4, p. 213.
- <sup>21</sup> P. Levy, H. Yand, M. Chshiev, and A. Fert, *Phys. Rev. B* **88**, 214432 (2013).
- <sup>22</sup> A. L. Ankudinov, B. Ravel, J. J. Rehr, and S. D. Conradson, *Phys. Rev. B* **58**, 7565 (1998).
- <sup>23</sup> C. Kittel, *Phys. Rev.* **73**, 155 (1948).
- <sup>24</sup> C. Hauser, T. Richter, N. Homonnay, C. Eisenschmidt, M. Qaid, H. Deniz, D. Hesse, M. Sawicki, S. G. Ebbinghaus, and G. Schmidt, *Sci. Rep.* **6**, 20827 (2016).
- <sup>25</sup> M. Haertinger, C. H. Back, J. Lotze, M. Weiler, S. Geprags, H. Huebl, S. T. B. Goennenwein, and G. Woltersdorf, *Phys. Rev. B* **92**, 054437 (2015).
- <sup>26</sup> C. Hahn, G. de Loubens, O. Klein, M. Viret, V. V. Naletov, and J. B. Youssef, *Phys. Rev. B* **87**, 174417 (2013).
- <sup>27</sup> H. Kurebayashi, O. Dzyapko, V. E. Demidov, D. Fang, A. Ferguson, and S. O. Demokritov, *Nat. Mater.* **10**, 660 (2011).
- <sup>28</sup> H. Wang, C. Du, P. C. Hammel, and F. Yang, *Appl. Phys. Lett.* **110**, 062402 (2017).